STScI | SPACE TELESCOPE SCIENCE INSTITUTE

Instrument Science Report STIS 2017-06

Updated Time Dependent Sensitivity Corrections for STIS Spectral Modes

Joleen K. Carlberg[1] & TalaWanda Monroe[1]

[1] Space Telescope Science Institute, Baltimore, MD

29 September 2017

ABSTRACT

The sensitivities of the STIS CCD and MAMA detectors have been slowly changing over time, and these changes vary with wavelength. The STIS time dependent sensitivity monitors track these changes, which must be corrected to allow accurate flux calibration and exposure time calculation. Here, we present updated calculations of the time dependent relationships using data obtained through mid-Cycle 24. We also retested the validity of applying the relationships derived with the lower resolution spectra to the medium resolution first order modes and echelle modes, for which we find reasonable agreement in most of the modes. As has been noted in the past, the G430M shows noticeably reduced sensitivity than the corresponding L-mode. At the 3165 Å cenwave setting, the sensitivity is also declining more rapidly than the corresponding L-mode. Direct comparison of the count rates obtained for the CCD's primary and secondary apertures also shows generally good agreement.

Contents

1. Introduction

There are two monitoring programs that track the sensitivity changes of the CCD and MAMA detectors of STIS in order to provide time dependent sensitivity (TDS) corrections to account for these changes. The TDS is the overall empirical throughput change of a particular observing mode after accounting for other known sensitivity variations, such as temperature dependent sensitivities and charge transfer inefficiencies in the CCD. The sensitivity changes are expected to have a wavelength dependency, and TDS relationships are measured in small wavelength bins across the spectra obtained with each of the low-dispersion gratings. The higher dispersion gratings (both the first order medium resolution gratings and the echelle gratings) adopt the TDS correction of the L-mode with the most similar wavelength coverage.

Historically, the TDS has been modeled with a segmented line model (Bohlin 1999) based on the expectation that the sensitivity should generally be slowly varying but that abrupt changes can occur if changes are made to the instrument operations (e.g., a change in the operating voltage) or if a rare, discrete event occurs (e.g., a new blemish on a grating). Holland (2014) developed a Python script to automate the process of finding the best breakpoints and fitting the slopes of the line segments. The TDS relationships currently in use in the pipeline were updated in 2009 (Goudfrooij et al. 2009), but recent sensitivity measurements are beginning to diverge from these relationships in some of the settings. Here, we present newly derived TDS relationships for all of the L-mode gratings. Although the Python code was designed to limit human intervention and thus provide an objective and "statistically rigorous" solution, we see evidence that the TDS measurements show variations that are not well-fit by the segmented line model. It is not apparent whether these variations arise in the observations themselves (e.g., slit placement errors) or in the analysis (e.g., underestimated uncertainties). Regardless, we found the need to change some of the hard-coded values in the Python script to achieve the fits we present here. Finally, we have computed TDS relationships for the higher dispersion settings and compared them to the relationships adopted from the low dispersion mode.

2. Data

2.1 Observations

The MAMA Spectroscopic Sensitivity Monitor makes repeated observations of three standard stars, GRW+70D5824 (L-modes), AGK+81D266 (M-modes), and BD+28D4211 (echelle modes), while the CCD Spectroscopic Sensitivity Monitor observes AGK+81D266 for all modes. All of the low resolution modes (G140L with the FUV-MAMA, G230L with the NUV-MAMA, and G230LB, G430L, and G750L with the CCD) are monitored every four months. Echelle modes are monitored approximately every three months, while the medium resolution modes are monitored less frequently, only once per year. For first order modes of the CCD, observations are taken at both the nominal position and at the E1 science aperture, which places the spectrum closer to the readout amplifier. The E1 aperture observations were a late addition to the monitoring program, and some modes only have E1 aperture TDS measurements after 2009 with less than a dozen observations total. Settings that have been monitored longer have anywhere from 25–90 observations.

Presently, only the TDS relationships derived using the low resolution mode observations are included in the reference files, and these relationships are applied to all higher resolution modes. The observations taken at higher resolution are used to verify that the application of the L-mode TDS is still valid. The signal-to-noise ratio (S/N) requirements are to achieve S/N of 50 per resolution element at the *least sensitive* wavelengths in the L-modes and S/N of 50 per resolution element at the central wavelengths for other modes. Additional lower S/N observations are available for the G430L grating, which are taken at different target position offsets in order to map the charge transfer inefficiency. Table 1 lists the program IDs of the calibration programs used in this ISR.

Cycle	CCD PID	MAMA PID
7	7672	7064, 7096, 7673
8	8418	8424
9	8856	8857
10	8914	8919
11	9627	9628
12	10030	10033
17	11401,11855	11403, 11860
18	12411	12414
19	12772	12775
20	13141	13145
21	13544	13548
22	13991	13994
23	14423	14429
24	14829	14833

Table 1. *Program IDs for the sensitivity monitors.*

2.2 Spectrum Preparation

The TDS analysis uses the net count rate column (NET) in the 1-dimensional extracted spectra fits file (the x1d.fits files) output by the *calstis* pipeline. In order to isolate the effects of the time sensitivity, the net count rates must first be corrected for the other known variable sensitivities that affect the count rate, including charge transfer inefficiencies (CCD only), red halo corrections (G750L grating only), and temperature dependent sensitivities (CCD and FUV-MAMA only). These tasks are accomplished in the Python script `tds_analysis.py` (Holland 2014) and approximate what is currently done in *calstis* in the flux calibration step. The long wavelength data (G750L and G750M) also exhibit substantial fringing; however, defringing is not currently corrected automatically in either *calstis* or by `tds_analysis.py`. This omission does not appear to have a significant effect, as the long wavelength TDS is the most well behaved.

The temperature sensitivity coefficients used in *calstis* are stored in the TDSTAB reference file along with the TDS slopes. The temperature correction is given as

$$\tau_{\rm c} = 1 + (T - \mathrm{REFTEMP}) \times \mathrm{TEMPSENS}, \tag{1}$$

and the net count rates are corrected by dividing by $\tau_{\rm c}$. The coefficients currently in use in `tds_analysis.py` were measured after the most recent TDSTAB files were delivered (see Holland et al., 2014, ISR 2014-02). They are listed in Table 2. Note the sign change for the FUV slope in Table 2 and in Equation 1 compared to ISR 2014-02 Table 3 and Equation 1. These differences are due purely to documentation error. Past temperature corrections have always been applied in the correct sense.

The echelle data require an additional processing step because there is evidence that the blaze function exhibits time and detector-position-dependent shifts (Aloisi 2006). Presently, the Python code circumvents this problem by fitting a polynomial to each echelle order, normalizing the spectra, and only utilizing the data between pixels 200

Detector	Optical Elements	REFTEMP (°C)	TEMPSENS ($^\circ C^{-1}$)	Start	Stop
FUV-MAMA	G140L, G140M, E140M, E140H, MIRFUV, MIRCUV	36.0	-0.0032	1997.38	Present
NUV-MAMA	G230L, G230M, E230M, E230H, MIRNUV, PRISM	None	None	1997.38	Present
CCD	G230LB, G230MB	19.0	0.0032	2001.5	Present
	G430L, G430M	19.0	0.0021	2001.5	Present
	G750L, G750M	19.0	0.0006	2001.5	Present
	MIRVIS	19.0	$f(\lambda)$[a]	2001.5	Present

Table 2. *Coefficients for the STIS temperature corrections, computed by Ralph Bohlin.*

[a] Adopts G230LB's TEMPSENS for $\lambda < 3000$ Å, G750L's for $\lambda > 5600$ Å, and G430L's for all other λ.

and 832, where the normalization is expected to be the best. However, the large scatter seen in the TDS measurements, which are much larger than the uncertainties, shows that more careful treatment of the data is necessary (see Section 4.3). Furthermore, the echelle observations taken post-SM4 also show occasional flux anomalies, or incidences of unusually low throughput ($\gtrsim 5\%$ losses), a phenomenon first noted in Bostroem et al. (2012).

2.3 Outliers

As was previously reported in the Cycle 21 close out report (Sana et al. 2015), two observations in Cycle 21 for the G750L setting appear to have discrepant fluxes that deviate from the general TDS trend. The L1 visit (Nov 27, 2013) shows a 1% flux decrease and L4 (Apr 16, 2014) shows a 12% decrease compared to both the L3 visit (Jul 24, 2014) and later Cycle 22 visits. As recommended in the close out report, the L4 visit for this grating was removed from the analysis, while the L1 visit was retained. There are examples of potential outliers in some of the other data sets, for example, the G140L observation on Mar 14, 2012 (see top panel of Figure 1). None of the apparent outliers had any obvious anomalies in their observation that could account for the reduced flux, and aside from the Cycle 21 L4 visit for G750L, all potential outliers were retained in the analysis.

3. TDS Analysis on L-modes

The `tds_analysis.py` code is described in detail in Holland (2014). Briefly, the corrected net count rates in each observation are summed over a large wavelength bin (see Table 1 of Holland (2014) for the definition of the wavelength bins). The relationship between the binned net count rates with time is iteratively fit with a segmented line model, progressing from a simple flat line, to a single line segment, to adding successively more breakpoints. An F-test is used to determine the preferred number of breakpoints (up to a user-imposed maximum), or the user can require a fixed number of breakpoints. At present, the user cannot manually place breakpoints. The analysis is then rerun on the same spectra on multiple small wavelengths bins, where the breakpoint times found in the "big bin" analysis are fixed, to allow the TDS slopes to have a wavelength dependence. The relationships are normalized such that the sensitivity in each wavelength bin is 1.0 at the reference time (year 1997.38 = MJD 50587.0) by definition. It is important to note that this normalization scheme means that an accurate fit in the vicinity of the reference time is essential to get an accurate TDS model. A poor fit at the reference time introduces a systematic over- or under-correction across the entire timeframe. An example "big bin" fit is shown in Figure 1, for the G140L grating, which spans 1150–1700 Å, together with the corresponding fit to one of the small wavelength bins spanning 1600–1650 Å.

For some modes, there is evidence that the sensitivity deviates from the simple segmented model by more than what is predicted by the error bars, as illustrated in

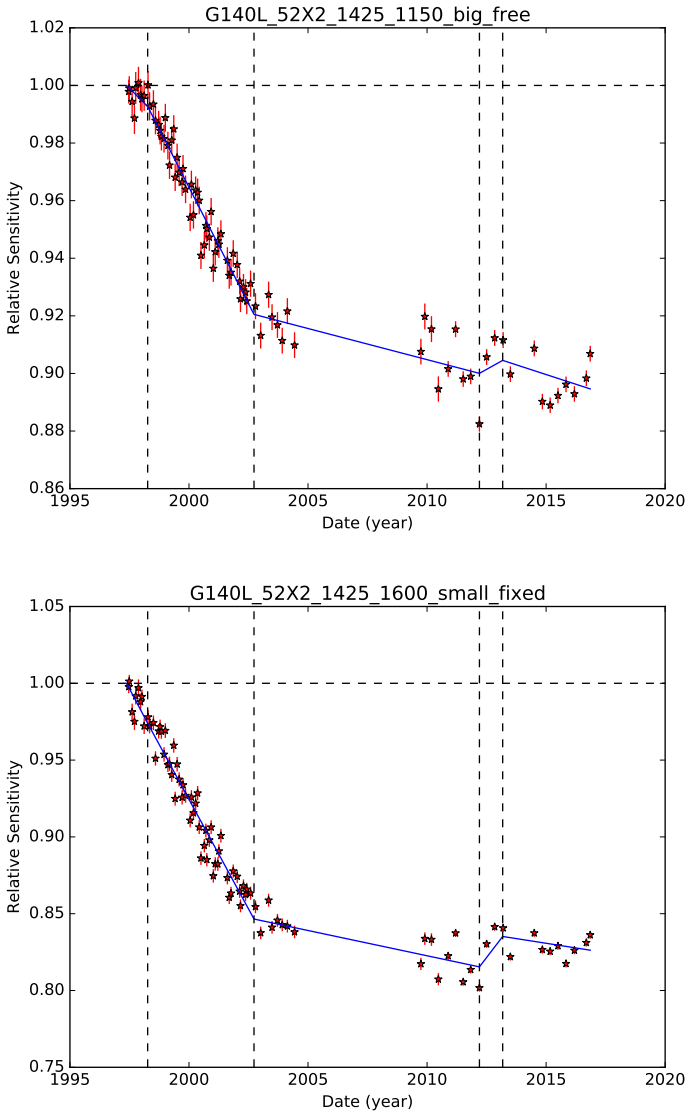

Figure 1. TDS fits for the G140L data utilizing the full wavelength range (top), which sets the breakpoints, and one of the small wavelength bins (bottom). The titles give the grating, aperture, central wavelength setting of the grating, beginning of the wavelength bin, bin size (big or small), and whether breakpoints were free or fixed parameters in the fit.

Figure 2, which shows the TDS fit and residuals of the G230L bluest wavelength bin. The error bars are only accounting for the Poisson variance in the counts, and the decrease in the error bars after about 2010 is due to the longer exposure times that were implemented. The consequence of the presumably underestimated error bars is that the mathematically favored models are those with many short line segments, particularly in more recent years where the time sampling is sparser and the error bars smaller. Working under the assumption that sensitivity does not exhibit numerous abrupt changes over short timescales, we were forced to implement some changes to the code.

The first change is implementing a scheme for requiring a minimum separation between successive breakpoint times ($\Delta t_{\rm min}$). Ideally, we would like to run the analysis with $\Delta t_{\rm min} \sim 1$ yr because we do not expect multiple abrupt changes to happen over one observing cycle. However, the underlying fitter, `mpfit.py`, has some limitations in how model parameter constraints are set. To enforce a minimum breakpoint time, the limits of the search space for each breakpoint must be defined such that there is a gap of $2\Delta t_{\rm min}$ between the search spaces for neighboring breakpoints. Thus it is possible

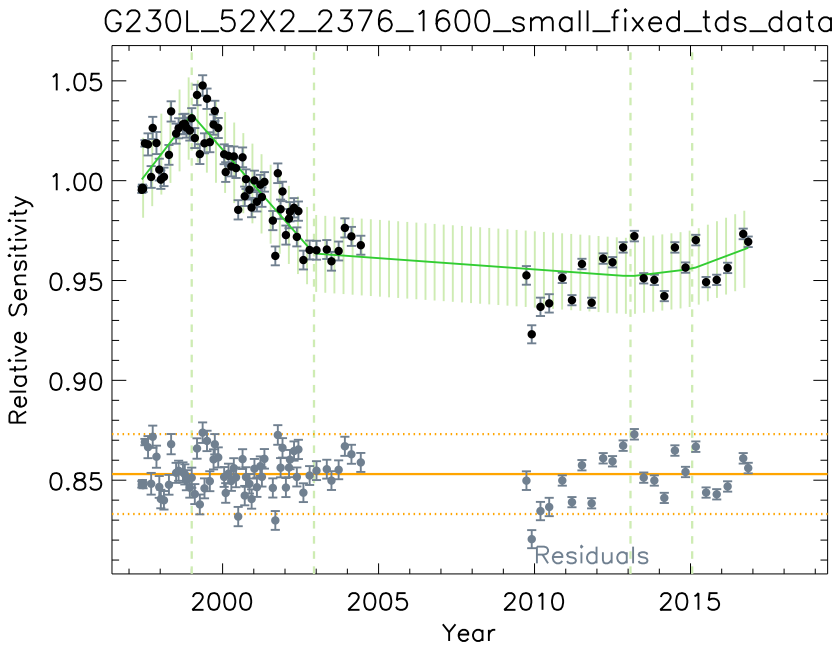

Figure 2. TDS fit for the G230L data in the 1600 Å wavelength bin. Dashed vertical lines mark the breakpoints, and the shading denotes $\pm 2\%$ around the fit. The residuals (plus an offset) are plotted near the bottom of the plot in gray, where the orange horizontal lines mark the x-axis and $\pm 2\%$ of the residuals plot.

for an ideal breakpoint time to be missed if it falls in one of these gaps. We found that setting $\Delta t_{\rm min}$ to 0.1 yr worked well.

The second change is to the upper limit allowed for the final breakpoint, which was previously hardwired to be 0.5 yr prior to the last observation. When one data point among the last few observations falls at the extreme distribution of the scatter, the model favors a solution with a breakpoint at the deviant point and occasionally leads to a solution with an extreme slope that we do not believe represents the true overall trend. Thus, the code was edited to require at least four observations on the final line segment. The G230L setting required further adjustment of the constraint to require at least 6 observations on the final line segment. In Figure 2, one can see that the last five points in this wavelength bin could be well fit with a rather steep line.

4. TDS Comparisons for Other Modes

We can test our assumption that the L-mode TDS relationships can be applied to the other spectroscopic gratings by running `tds_analysis.py` on the higher resolution data and comparing the fits. Recall that the normalization of both the TDS data and the fits is defined so that the TDS function is exactly 1.0 at the reference time. Therefore, the relative scaling between two different TDS models can be influenced by a poor fit to the data at early times. In the next few sections we discuss the results of these comparisons.

4.1 Single Order M-modes

Figures 3 and 4 show the TDS fits to the single order data of the eight different grating and central wavelength combinations that are monitored. The shading around each fit shows $\pm 2\%$ to give a sense of how well the two fits agree. Generally, we find very good agreement between the fits to the M-mode data and the L-mode fits that will be applied with the TDS reference file, and we do not find sufficient disagreement between them to justify calculating TDS relationships from the M-mode data directly. Nevertheless, there are a few mismatches that are worth discussing:

G140M λ1173 (top left in Figure 3): The earliest data set comes after the first breakpoint found in the L-mode fit, so it is possible that the steep decline in sensitivity seen in the M-mode data was also flatter at times earlier than 1998.5. Unfortunately, this uncertainty in the behavior of the sensitivity at the reference time affects the overall scaling. If the M-mode sensitivity does have a similar early-time breakpoint as the L-mode, then the scaling of both the data points and the M fit (purple) would move up in this plot, which would bring the two different TDS fits into better agreement at times before 2002. However, that same shift would cause worse agreement between the two TDS fits after 2009.

G140M λ1567 (top right in Figure 3): The most recent TDS data point suggests that the sensitivity is falling much more steeply than what is predicted by the L-mode fit. However, if that single observation is ignored, the last segment of the M-mode fit would be much flatter and be in good agreement with the L-mode fit. We will monitor

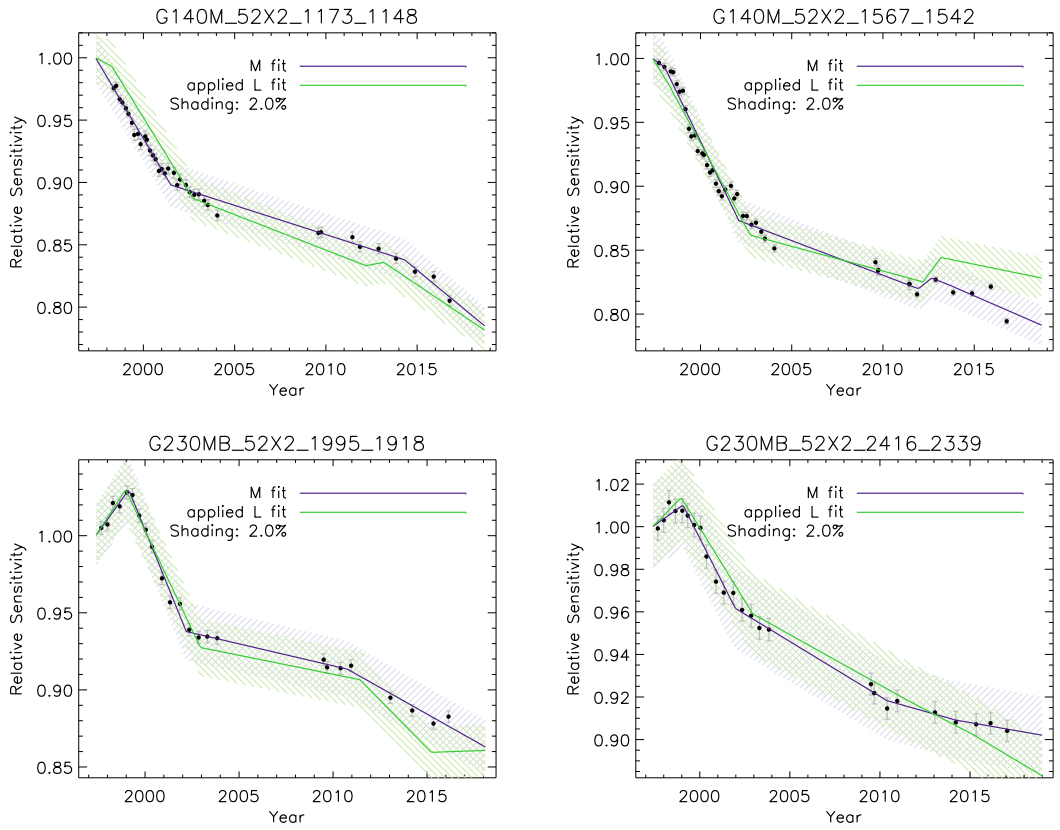

Figure 3. TDS for single-order, medium resolution data, ordered by central wavelength (part 1). The fit to the M-mode data is shown in purple, and the data points have been scaled by that fit. The L-mode fit that will be applied to the data with the reference file is shown in green.

the new data taken with this setting to see determine whether the 2016.78 point is an outlier or if the sensitivity of this mode is truly falling off more steeply.

G430M λ3165 (top right in Figure 4): The data for this grating suggest that the sensitivity showed a sharp decline in sensitivity around the year 2000 that was not seen in the G430L grating and that the sensitivity continues to fall more steeply. The incoming data over the next few months to years will determine whether this trend continues. If so, it may prove necessary to compute the TDS correction for this grating independently.

4.2 E1 positions

Starting in Cycle 11, the TDS monitoring program began taking CCD data with the target centered at both the primary aperture location and at the "E1" science aperture location. The latter aperture is used to place the spectrum closer to the readout amplifier to minimize the effects of charge transfer inefficiency (CTI), which on STIS smears out

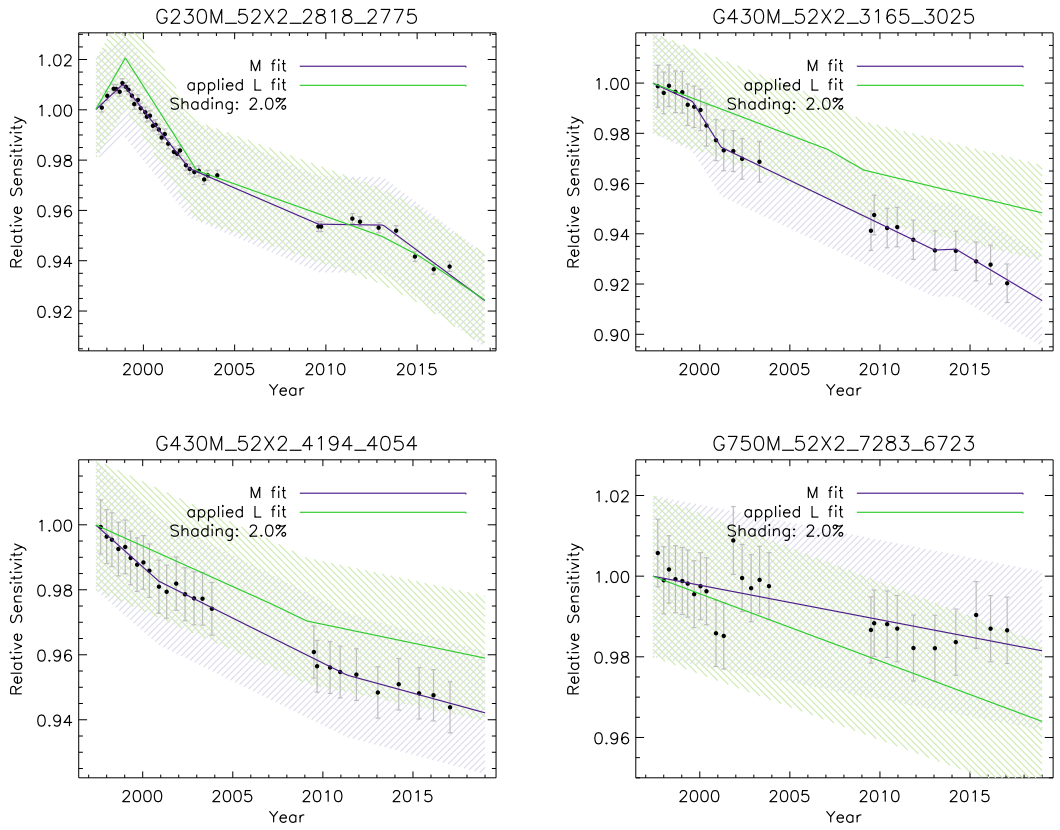

Figure 4. TDS for single-order, medium resolution data, ordered by central wavelength (part 2).

charge parallel to the readout axis (Goudfrooij et al. 2006). CTI is an especially pernicious problem for faint objects, and the E1 aperture is recommended for faint objects to mitigate CTI. We use the available E1 observations to test whether the TDS of the E1 aperture position is the same as the primary aperture position. Without any data prior to $\sim$2002, it is impossible to compute an independent TDS fit for these data because there is no constraint on the behavior of the sensitivity at early times. Instead, we directly compare the count rates of the observations of the same object and spectroscopic setting taken at both the primary and secondary aperture. This comparison is valid because the only variable that differs between the observations is a small change of the pointing of the telescope to place the dispersed light at a different position on the detector, and the CTI correction described in Goudfrooij et al. (2006) is applied by `tds_analysis.py`.

We have eight different grating and central wavelength combinations, three L-mode and five M-mode. As in the previous analyses, we computed TDS measurements (i.e., binned count rates) in each of the "small" wavelength bins defined for the L-mode data. Figure 5 shows the distribution of count rate agreement between observations taken at the primary and E1 science positions. The G750L λ7751 grating is plotted

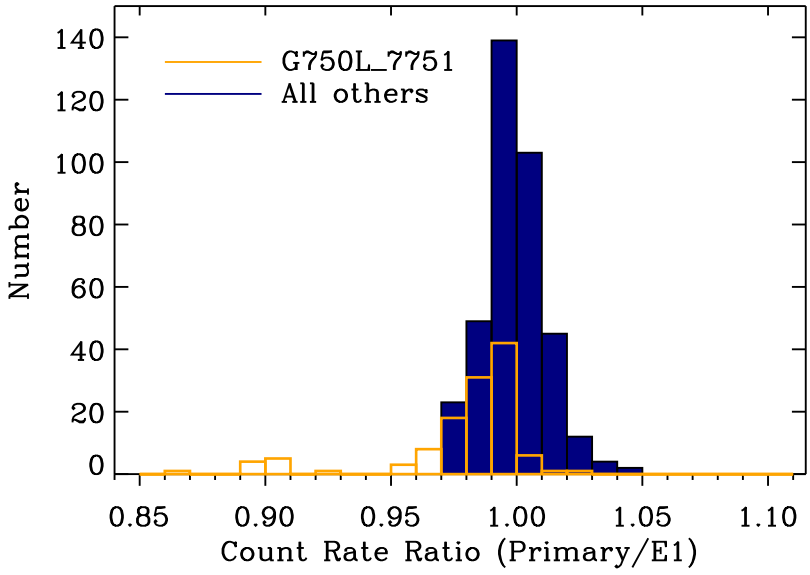

Figure 5. Ratio of the count rates of observations taken at the primary science aperture and a nearly contemporaneous observation of the same target at the E1 science aperture with the same grating and central wavelength. Results from the G750L λ7751 grating are plotted separately to illustrate the larger spread.

separately from the rest because it requires special consideration. In general, we find the agreement to be within a few percent (RMS $=$ 2.1% including G750L and 1.2% without). This good agreement gives us confidence both that the TDS is independent of where the spectrum is recorded on the CCD and that the CTI correction is working well. The G750L λ7751 grating shows the largest discrepancies, particularly at the longest wavelength bins where a number of effects may be at play. The most likely culprit for the discrepancy is the uncorrected fringe patterns, which vary with detector position and have the largest amplitudes at the reddest wavelengths. The STIS CCD also exhibits a "red halo" that complicates the CTI correction, and the G750L λ7751 discrepancies may be pointing to a need to improve the CTI correction at the longest wavelengths.

4.3 Echelle Modes

In addition to testing the applicability of using the L-mode derived TDS functions on first order M-modes and alternative aperture positions, we also wanted to test the applicability to the echelle modes. Unfortunately, some spectral orders show large scatter in the TDS measurements made for the echelle data, raising the question of whether the count rates measured in the code are accurate. One example of this large scatter is given in Figure 6. The scatter in the data at times after 2010 is roughly twice as large as the scatter seen in the G230L data shown in Figure 2.

One known contributor to the scatter is the echelle flux anomalies, which are observations that show spurious throughput losses of 5–10% (Bostroem et al. 2012). Another potential contributor to the scatter is the treatment of the blaze function, an optical effect that modulates the intensity of the spectrum in each echelle order as a function of the observed wavelength. The characteristic shape of the blaze yields relatively high sensitivity in the middle of each spectral order and lower sensitivity that declines steeply at the order edges. Although the shapes of the blaze functions have been characterized for STIS, the positions of the blaze functions for the echelle modes are known to shift with time (Aloisi 2006).

The present treatment of the blaze function in the TDS code does not utilize the known shapes and shifts of the blaze functions, which are used in the *calstis* pipeline. Instead, the code simply normalizes each spectral order with a low order polynomial and measures the count rate over the central region (pixels 200–832). Although this method circumvents the potential errors introduced by the uncertainty in the time dependent shifts of the blaze, it does introduce other new sources of uncertainty. There is no weighting to account for the fact that the S/N is higher in the center of the spec-

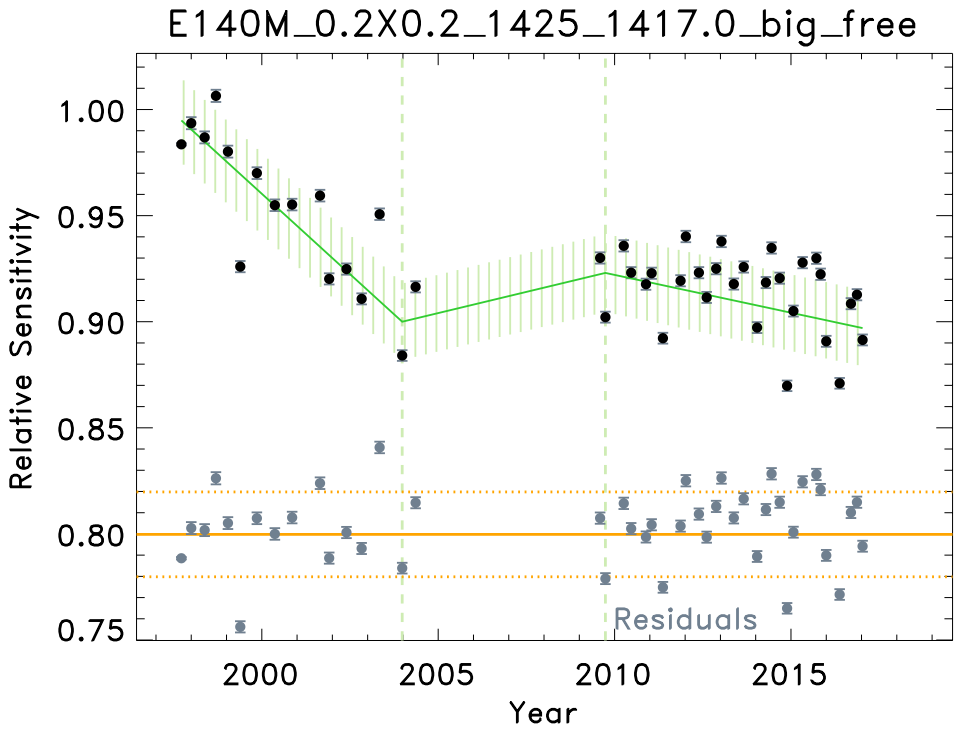

Figure 6. An example of the TDS and residuals calculated for one spectral order of the E140M grating, illustrating the larger scatter in the TDS measurements around the best fit.

trum than at the edges of the spectrum. Furthermore, the spectrum of BD+28D4211 exhibits some deep absorption features that can strongly affect the polynomial fit to the continuum. It is possible that the continuum fits in orders with these deep absorption features are dramatically different between observations. These factors must be investigated further before we can test whether applying the L-mode derived TDS corrections are sufficiently accurate for correcting the echelle data.

5. Reference File Update

New TDS reference files were delivered on March 10, 2017. There is one TDS references file per detector (FUV-MAMA, NUV-MAMA, and CCD), and each file contains the following information about the TDS for each optical element associated with the detector: number of break points, breakpoint times, number of wavelength bins, center wavelength of the bin, and a slope for each combination of wavelength center and breakpoint time. Table 3 lists all of the optical elements specified in the reference files, their wavelength coverage, and which TDS relationship it inherits. The tables documenting the fitted parameters for each L-mode grating and wavelength bin are in Appendix A. The breakpoint times, which are used for all wavelength bins of a particular grating, are given in Table 4, while the slopes of each line segment for each wavelength bin are given in Tables 5–9. The remainder of this section documents special cases in the reference files.

5.1 Imaging Modes

The imaging modes (optical elements beginning "MIR") are also corrected for the TDS; Roman-Duval & Proffitt (2013) demonstrated that the flux measured in standard star fields with these corrections in place are accurate to $< 1\%$. The MIRVIS optical element has a complicated update since it combines the TDS relationships of three different gratings: G230LB, G430L, and G750L. The reference files allow only one set of breakpoint times to be defined for a given optical element, and we adopt the times associated with G230LB for MIRVIS. Because the G750L grating is fit by a single line segment, the slope of that line can simply be specified at each of the five breakpoint times for the overlapping wavelength bins of MIRVIS. The G430L setting, however, is fit by three line segments, which need to be mapped onto the five MIRVIS line segments defined by the G230LB breakpoint times. We adopted the following procedure. For each wavelength bin, the G430L segment #1 slope is adopted for the first three line segments, and the G430L line segment #3 slope is adopted for the fourth and fifth line segments. The exception is for wavelength bins 3600 Å and 4400 Å, where the G430L segment #1 slope is adopted for only the first two line segments, and the G430L segment #3 slope is adopted for the remaining three line segments. The G430L segment #2 slope is not used to define the MIRVIS TDS for any wavelength bin.

Detector	Optical Element	λ Coverage (Å)	$\Delta\lambda$ (Å)	Inheritance
FUV-MAMA	G140L	1175–1675	50	G140L
	G140M	1175–1675	50	G140L
	MIRFUV	1175–1975[a]	50	G140L
	MIRCUV	1175–1975[a]	50	G140L
	E140M	1125–1725	50	G140L
	E140H	1125–1725	50	G140L
NUV-MAMA	G230L	1650–3050	100	G230L
	G230M	1650–3050	100	G230L
	MIRNUV	1150–3750[a]	100	G230L
	E230M	1550–3150	100	G230L
	E230H	1550–3150	100	G230L
	PRISM	1150, 10880		None[b]
CCD	G230LB	1750–2950	100	G230LB
	G230MB	1750–2950	100	G230LB
	G430L	3000–5600	200	G430L
	G430M	3000–5600	200	G430L
	G750L	5700–9700	400	G750L
	G750M	5700–9700	400	G750L
	MIRVIS	1650–2950,	100	G230LB
		3000–5600,	200	G430L[c]
		5700–9700[d]	400	G750L

Table 3. *TDS Inheritance*

[a] Additional wavelength entries in TDS reference file at 10780 and 10880 Å.

[b] An independent TDS correction has been derived for the PRISM by Maiz-Apellaniz & Bohlin (2005) for pre-SM4 observations. No TDS is supplied for post-SM4 observations.

[c] See Section 5.1 for details on how G430L TDS relationship is applied to MIRVIS.

[d] Additional wavelength entries in TDS reference file at 9800, 9900, 10100, and 10450 Å.

5.2 PRISM

Maiz-Apellaniz & Bohlin (2005) found an independent TDS relationship for PRISM observations, based on data taken from 1998–2004. Their piece-wise fit suggested a flat slope for post-2004 data, and they adopted a single-line fit (not the piece-wise segments) for pre-2004 observations. Since then, only one standard star observation has been made since STIS resumed operations after the side 1 electronics failure. We compared the flux of HS2027+0651 observed on 2009-09-03 (ob8708020) to that of the 2003-11-10 (o8v540060) observations under two assumptions for the TDS: extrapolating the slope fit to the pre-2004 data, and assuming the slope flattens at MJD = 53077.0. Both assumptions yield fluxes deviating by $\sim 5\%$ from the 2003 data, though in opposite directions. We adopt the latter assumption (no additional sensitivity changes) in the TDS reference file since we have insufficient data to constrain the rate of change after SM4. Because the PRISM has not been utilized for science observations since SM4,

improving its calibration has remained at low priority. Potential users should be aware that its sensitivity is presently unknown to the level of $\sim 25\%$.

6. Recommendations

Recommendations related to observations:

- Investigate whether the G430M setting should have its own TDS fit measured, rather than inheriting the G430L TDS.
- Compare absolute fluxes for all modes against the flux standard model to ensure there are no systematic offsets in the output fluxes.
- Investigate the source of the large scatter seen in the echelle TDS measurements.
- Investigate structure in TDS residuals.
- Investigate source of G750L count rate discrepancies between primary and E1 aperture positions.
- Consider adding fringe corrections for the G750L/M settings (low priority).
- Obtain new measurements of the white dwarf HS2027+0651 with the PRISM to measure a post-SM4 TDS slope (low priority).

Recommended changes to the TDS fitting algorithms in `tds_analysis.py`

- Update the error to include more than just the Poisson errors, e.g., uncertainties introduced by the CTI correction and temperature dependent sensitivity correction.
- Better treatment of echelle normalization:
  - Mask known deep absorption features that can affect the polynomial fits to the continuum.
  - Clip the unused edges of the echelle orders by *wavelength* instead of by *pixel*.
  - Compute a weighted average of the TDS using the S/N, which varies across even a single echelle order, as the weight.
- Allow independent fits to pre- and post-SM4 data, with the ability to input previously determined pre-SM4 fits to allow a static solution to pre-SM4 data when future updates to new epochs are required.
- Add ability to rerun the fitting without re-processing all of the input spectra.
- Upgrade the code to be compatible with Python 3.5.

- Add ability to flag and optionally remove highly-deviant TDS measurements.
- Consider adding constraints on how much the slope of one line segment can deviate from the previous slope.
- Substitute the underlying fitter (currently `mpfit.py`) to one that allows specifying relational constraints (e.g., $t_{\mathrm{BP},i} > t_{\mathrm{BP},i-1} + \Delta t_{\mathrm{min}}$) OR rewrite the model representation to achieve this behavior with `mpfit.py`.

Change History for STIS ISR 2017-06

Version 1: 29th September, 2017- Original Document

References

Aloisi, A. 2006, The 2005 HST Calibration Workshop: Hubble After the Transition to Two-Gyro Mode, 190
Bohlin, R. 1999, STIS ISR, 1999-07
Bostroem, K. A., et al. 2012, STIS ISR, 2012-01
Goudfrooij, P., et al. 2006, PASP, 118, 1455
Goudfrooij, P., et al. 2009, STIS ISR, 2009-02
Holland, S. T., et al. 2014, STIS ISR 2014-02
Holland, S.T. 2014, STIS TIR, 2013-03
Maiz-Apellaniz, J., & Bohlin, R. C. 2005, STIS ISR 2005-01
Roman-Duval, J. & Proffitt, C., 2013, STIS ISR 2013-02
Sana, H. et al., 2015. STIS ISR 2015-09

Appendix A

Detector	Optical Element	Segment #	MJD	Year
FUV-MAMA	G140L	1	50587.00	1997.38
		2	50910.05	1998.26
		3	52541.41	2002.73
		4	55999.88	2012.20
		5	56356.68	2013.18
NUV-MAMA	G230L	1	50587.00	1997.38
		2	51182.65	1999.01
		3	52614.00	2002.93
		4	56320.16	2013.08
		5	57042.12	2015.05
CCD	G230LB	1	50587.00	1997.38
		2	51166.24	1998.97
		3	52619.29	2002.94
		4	55714.98	2011.42
		5	57104.57	2015.22
CCD	G430L	1	50587.00	1997.38
		2	54141.64	2007.11
		3	54866.77	2009.10
CCD	G750L	1	50587.00	1997.38

Table 4. *Breakpoint times that define the beginning of each line segment, given for each L-mode setting.*

Optical Element	Wavelength	Slope 1	Slope 2	Slope 3	Slope 4	Slope 5
FUV−MAMA/G140L	1175.0	−0.7647	−2.3764	−0.5687	0.2746	−0.9861
	1225.0	−4.3821	−0.6846	−0.2303	0.0073	−0.0371
	1275.0	−0.4309	−0.9952	−0.0866	0.4243	−0.3218
	1325.0	0.1737	−1.2330	−0.1160	0.5167	−0.1842
	1375.0	0.2303	−1.3216	−0.1903	0.4584	−0.3905
	1425.0	0.2529	−1.9847	−0.2321	−0.2358	−0.0044
	1475.0	−1.8805	−2.1275	−0.3396	1.2541	−0.5383
	1525.0	−2.2176	−2.4141	−0.3836	1.1947	−0.3168
	1575.0	−2.3178	−2.6366	−0.3863	1.9573	−0.2915
	1625.0	−2.9432	−2.8532	−0.3290	2.0271	−0.2432
	1675.0	1.9289	−3.0070	−0.3462	1.2803	−0.1914

Table 5. *TDS slopes (%/yr) of each line segment in the 11 wavelength bins of G140L*

Optical Element	Wavelength	Slope 1	Slope 2	Slope 3	Slope 4	Slope 5
NUV−MAMA/G230L	1650.0	2.0313	−1.7757	−0.1128	0.1890	0.5874
	1750.0	1.1307	−2.0272	−0.0912	−0.2683	0.2244
	1850.0	1.9804	−2.2612	−0.0882	−1.2978	0.5958
	1950.0	2.6631	−2.5628	−0.0786	−1.9460	0.6607
	2050.0	1.4172	−2.3826	−0.1685	−1.7211	0.4827
	2150.0	1.8155	−2.2878	−0.2008	−1.3518	−0.0782
	2250.0	2.3216	−2.1321	−0.2006	−0.8572	−0.4695
	2350.0	0.4194	−1.5851	−0.3070	−0.5463	−0.2978
	2450.0	1.3547	−1.6232	−0.3352	−0.6714	0.0632
	2550.0	−0.4284	−1.0607	−0.3496	−0.4047	−0.0197
	2650.0	0.8746	−1.2552	−0.3117	−0.6092	−0.0405
	2750.0	0.6258	−1.0027	−0.2601	−0.4169	−0.0604
	2850.0	1.2670	−1.1431	−0.2582	−0.3801	−0.4856
	2950.0	0.2127	−0.8327	−0.2325	−0.3556	−0.5577
	3050.0	1.5300	−1.0539	−0.2162	−0.3665	−0.2454

Table 6. *TDS slopes (%/yr) of each line segment in the 15 wavelength bins of G230L*

Optical Element	Wavelength	Slope 1	Slope 2	Slope 3	Slope 4	Slope 5
CCD/G230LB	1750.0	1.1756	−2.3100	−0.3223	0.0335	−0.5936
	1850.0	2.9942	−2.7233	−0.1815	−0.7733	−0.0782
	1950.0	1.8857	−2.5744	−0.2462	−1.2386	0.0428
	2050.0	1.6593	−2.4884	−0.2667	−1.1360	−0.5455
	2150.0	0.8263	−2.0955	−0.4087	−0.6268	−0.8447
	2250.0	0.9705	−1.9092	−0.4567	−0.3961	−0.6258
	2350.0	0.7774	−1.6317	−0.4814	−0.3922	−0.7744
	2450.0	0.8605	−1.3733	−0.4727	−0.4434	−0.5060
	2550.0	0.4923	−1.1642	−0.4861	−0.2672	−0.7738
	2650.0	0.4448	−1.0957	−0.4144	−0.3523	−0.5176
	2750.0	0.7843	−1.0587	−0.4129	−0.2893	−0.5233
	2850.0	−0.2480	−0.7593	−0.4309	−0.3291	−0.7717
	2950.0	−0.2859	−0.7665	−0.4545	−0.1440	−0.7219

Table 7. *TDS slopes (%/yr) of each line segment in the 13 wavelength bins of G230LB*

Optical Element	Wavelength	Slope 1	Slope 2	Slope 3
CCD/G430L	3000.0	−0.3256	−0.1433	−0.2435
	3200.0	−0.2717	−0.4111	−0.1723
	3400.0	−0.2699	−0.1854	−0.1882
	3600.0	−0.3615	−0.0951	−0.0523
	3800.0	−0.3333	−0.1806	−0.2228
	4000.0	−0.1722	−0.5505	−0.1131
	4200.0	−0.2494	−0.2670	−0.1157
	4400.0	−0.4052	0.1053	−0.0706
	4600.0	−0.2356	−0.4370	−0.2063
	4800.0	−0.2175	−0.4360	−0.1616
	5000.0	−0.2243	−0.3048	−0.1720
	5200.0	−0.2856	−0.2008	−0.1460
	5400.0	−0.3090	−0.1673	−0.1607
	5600.0	−0.2778	−0.3510	−0.1599

Table 8. *TDS slopes (%/yr) of each line segment in the 14 wavelength bins of G430L*

Optical Element	Wavelength	Slope 1
CCD/G750L	5700.0	−0.1103
	6100.0	−0.1437
	6500.0	−0.1573
	6900.0	−0.1666
	7300.0	−0.1792
	7700.0	−0.1960
	8100.0	−0.1673
	8500.0	−0.2726
	8900.0	−0.2942
	9300.0	−0.2812
	9700.0	−0.3661

Table 9. *TDS slopes (%/yr) of each line segment in the 11 wavelength bins of G750L*